Earth and Planetary Science Letters 580 (2022) 117387

Contents lists available at ScienceDirect

Earth and Planetary Science Letters

www.elsevier.com/locate/epsl

Evidence for basalt enrichment in the mantle transition zone from inversion of triplicated P- and S-waveforms

Felix Bissig [a,*], Amir Khan [a,b], Domenico Giardini [a]

[a] Institute of Geophysics, ETH, Zürich, Switzerland
[b] Physik-Institut, University of Zürich, Zürich, Switzerland

ARTICLE INFO

Article history:
Received 5 July 2021
Received in revised form 11 January 2022
Accepted 14 January 2022
Available online xxxx
Editor: H. Thybo

Keywords:
triplicated body waves
mantle transition zone
thermochemical structure
mantle equilibration
waveform modeling
inversion

ABSTRACT

Recycling of chemically stratified oceanic lithosphere at subduction zones and mantle mixing is the main source for the production and long-term maintenance of heterogeneities as evidenced through mantle samples and the presence of seismic scatterers. The mantle transition zone (MTZ), which is bound by seismic discontinuities around 410 and 660 km depth that reflect mantle mineral phase transformations in the olivine system, is considered to play a significant role in reprocessing and remixing of subducted oceanic plates. However, the compositional nature and mixing state of the MTZ is generally unconstrained with models ranging from a fully-equilibrated pyrolitic to a mechanically-mixed MTZ enriched in basalt. Here, we consider regional P- and S-waveforms from different regions that have interacted extensively with the MTZ and are triplicated at the seismic discontinuities. Because of the strong interaction with the MTZ and the sensitivity to mantle temperature and composition, triplicated waveforms can be used as probes of the thermochemical conditions in and around the MTZ. Here, we model the MTZ by considering two-endmember models: a fully-equilibrated and a mechanical mixture of depleted (harzburgite) and fertile (basalt) lithologies, whose properties are computed self-consistently using petrologic phase equilibria in combination with equation-of-state modeling as a function of pressure, temperature, and composition. Based on this method, we invert carefully selected triplicated P- and S-waveforms for local one-dimensional profiles of MTZ structure. In some of the studied regions, we find both radial and lateral heterogeneities in composition that show a trend from more fertile lithologies in the mid-MTZ to more pyrolitic compositions below the MTZ. This is in line with evidence provided by global geodynamic models that support the segregation and accumulation of basalt toward the mid-MTZ. Because a number of the regions studied here encompass subduction zone settings, we also observe lower-than-average mantle temperatures (∼1200°C) and, as a consequence, thicker-than-average MTZ (∼240–280 km). While some areas appear to be better fit with a particular mixing model, rigorous statistical analysis of the datafit shows that on average, and at the level of the resolving power of the data, an equilibrated mantle across a large part of the studied subduction zone settings is favored.

1. Introduction

Chemical segregation of basaltic melt from the depleted harzburgitic residuum at mid-ocean ridges leads to a stratified oceanic lithosphere, which continuously cools, thickens, and ultimately gets subducted back into the mantle. The downwelling of cold material at plate boundaries is, alongside hot rising plumes, the key geodynamic process governing the heat and mass exchange between the upper and lower mantle (e.g., Silver et al., 1988). The remnants of subducted oceanic crust and lithosphere are probably the primary source of the seismically observed heterogeneities in the Earth's mantle across several scales that include sub-wavelength heterogeneities affecting absolute seismic velocities (e.g., Xu et al., 2008), km-sized scatterers (e.g., Kaneshima, 2016), and 1000-km large anomalies associated with transition zone topography and provinces of material at the core-mantle-boundary (e.g, Ishii and Tromp, 1999). This geophysical image of a heterogeneous mantle is further supported by the geochemical analysis of erupted lavas, that indicate distinct mantle reservoirs differing in isotopic and trace element signatures (e.g., White, 2010) and also in major element compositions (Jackson and Dasgupta, 2008). A key role in the processing of subducted oceanic plates is assigned to the mantle transition zone (MTZ), which is demarcated by seismic discontinuities that occur globally around

* Corresponding author.
E-mail address: felix.bissig@erdw.ethz.ch (F. Bissig).

https://doi.org/10.1016/j.epsl.2022.117387
0012-821X/

410 and 660 km depth (e.g., Helffrich, 2000). These discontinuities reflect mineral phase transformations of olivine→wadsleyite (the 410-km discontinuity) and ringwoodite→bridgmanite+ferropericlase (the 660-km discontinuity) (Ringwood, 1975), respectively.

On account of the distinct phase transformations of harzburgite and basalt within a slab, a density crossover is predicted at the base of the MTZ that, combined with the rheologically-induced segregation of basalt and harzburgite (Karato, 1997), is postulated to enrich the MTZ in basalt (e.g., Irifune and Ringwood, 1993). Such a compositionally fertile MTZ is often seen in geodynamic simulations (e.g., Ballmer et al., 2015; Yan et al., 2020), while lateral and radial variations in mantle composition are supported by seismic studies on both global and continental scale (e.g., Cammarano et al., 2009; Khan et al., 2009; Wu et al., 2019; Munch et al., 2020; Bissig et al., 2021). Yet, the nature and the level of mixing within the MTZ remains enigmatic. With seismic tomography images (e.g., Schaeffer and Lebedev, 2013) that show subducted oceanic plates penetrating into the lower mantle in some regions, while stagnating in the MTZ in others, mixing likely encompasses the entire spectrum ranging from fully-equilibrated pyrolite (e.g., Weidner, 1985) to a mechanically-mixed MTZ enriched in basalt (e.g., Agee, 1993; Cammarano et al., 2009). The sporadic passage of slabs through the MTZ, in turn, suggests that mantle convection cycles intermittently between layered and whole-mantle mode, while a globally-averaged compositional stratification at the boundary between the MTZ and the lower mantle is maintained (Tackley, 2000). In support hereof, the global joint short- and long-period seismic study of Munch et al. (2020) found that chemical equilibration appears less pervasive beneath cratons than elsewhere, implying that the mantle underneath could be isolated from entrainment associated with the background mantle flow.

To investigate the extent to which the MTZ is compositionally and thermally equilibrated on regional-to-global scales, we consider regional P- and S-waves that turn at depths between ∼200–800 km and, as a consequence, have spent a significant part of their trajectory in the MTZ. Through their extensive interaction with the MTZ, regional waves carry a wealth of information and are ideal for studying MTZ structure (e.g., Stähler et al., 2012; Li et al., 2022). Converted waves (receiver functions; e.g., Tauzin et al., 2008; Munch et al., 2020) and underside reflections (PP- and SS-precursors; e.g., Tian et al., 2020) are primarily sensitive to the depth and amplitude of discontinuities. In contrast, regional body waves sample the MTZ from top to bottom (with epicentral distance) and hence convey a more continuous picture of MTZ structure. The first attempts to exploit the properties of triplicated waves to derive regional seismic velocity models date back to the 1960s (e.g., Niazi and Anderson, 1965). Subsequently, various approaches have been employed, including fitting synthetic to observed waveforms via trial-and-error (e.g., Tajima et al., 2009) and direct inversion (e.g., Grand, 2002; Borgeaud et al., 2019). Here, we extend our previous work (Khan et al., 2009; Munch et al., 2020; Bissig et al., 2021) to inversion of regional P- and S-waveforms for MTZ structure. To base our interpretations of the results on sound inference, we make use of statistical analysis to obtain quantitative measures of information content and the statistical significance of the results through Bayesian hypothesis testing.

2. Materials and methods

2.1. Triplicated body waves

P- and S-waves from regional events turn in the depth range ∼200–800 km within the mantle and are recorded at epicentral distances between $10^\circ - 30^\circ$. As a result of the discontinuities in seismic wave velocities at ∼410 and ∼660 km depth (hereinafter referred to as '410' and '660', respectively), three arrivals, corresponding to direct, reflected, and refracted arrivals, are seen within a short time window at these distances (cf. Fig. 1A). For each discontinuity, the P- and S-wave travel time curves span three distinct branches corresponding to the direct, reflected, and refracted arrivals. This is referred to as "triplication" and is illustrated in Fig. 1B and C, showing travel times and corresponding P- and S-waveform sections, respectively, in the regional distance range for model IASP91 (Kennett and Engdahl, 1991). Observing distinct triplicated branches in the waveforms also depends, in addition to velocity structure, on the length of the source time function (STF) and the frequency band studied. For S-waves, differential travel times are longer because of lower velocities relative to P-waves, which is why triplicated S-waves are better discriminated (cf. Fig. 1B and C) at the typical periods studied here (5–30 s).

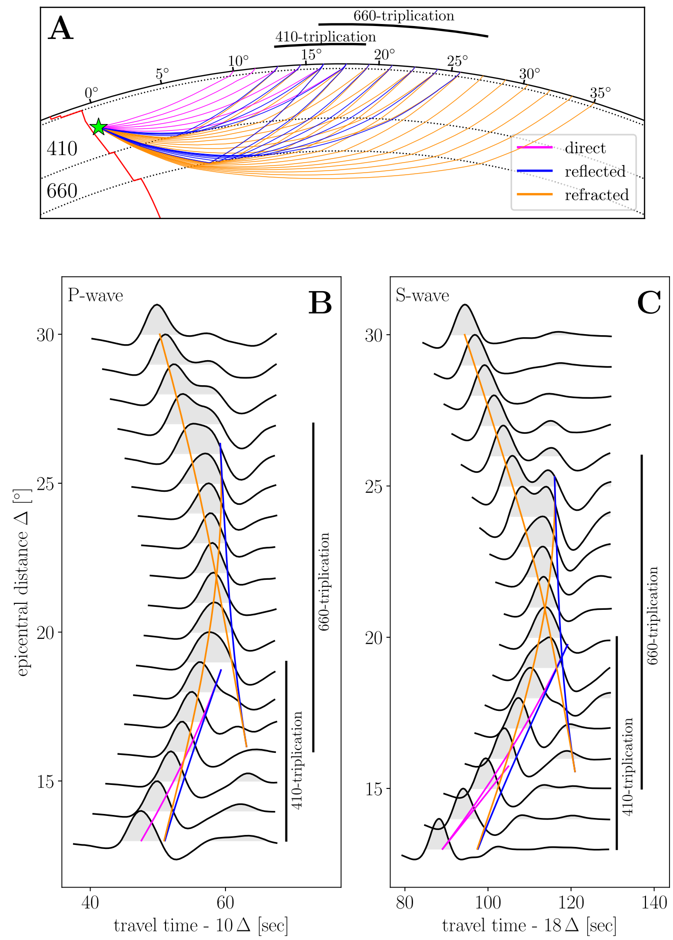

Fig. 1. Ray paths and waveforms of triplicated body waves. (**A**) Illustration of the raypaths taken by the direct, reflected, and refracted branches of a P-wave being triplicated at the 410 and 660 discontinuities (dotted lines) using the seismic reference model IASP91 (red; Kennett and Engdahl, 1991). The source is located at a depth of 195 km (green star) and the focal mechanism of event A5 (cf. Table S.1) is used to compute synthetic P- (**B**) and S-wave (**C**) sections, respectively. P- and S-waveforms are filtered between 5–30 s and 8–30 s, respectively. Travel time curves in (**B**) and (**C**) are color-coded according to the respective rays in (**A**). Black lines indicate the distance ranges over which the 410- and 660-triplicated phases are seen.

2.2. Event selection

Optimal source-receiver configurations for the study of triplicated waves are seismic networks covering regional epicentral distances (10–30°) from relatively deep seismic events related to the circum-pacific subduction system. We have compiled a data set of triplicated P- and S-waveform sections from different regions of the Earth to study the MTZ structure (Fig. 2A; Table S.1).

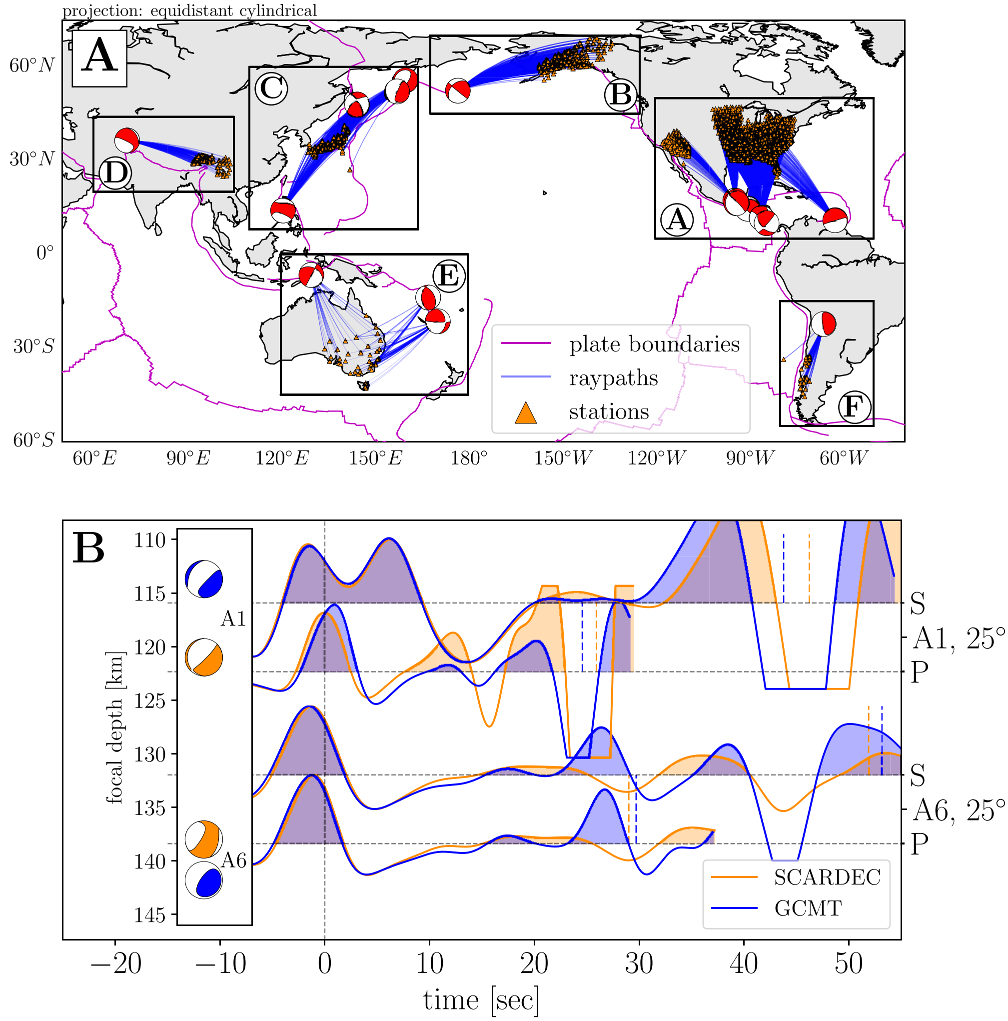

Fig. 2. Geographical distribution of events and receivers (**A**) and synthetic waveforms (**B**). (**A**) Map displaying event locations (beachballs at epicentre represent focal mechanisms), stations (orange triangles), and raypaths (blue) for the 6 regions considered in this study (A–F). Plate boundaries from USGS are plotted in magenta. More event details can be found in supplementary Table S.1. (**B**) P- and S-wave Instaseis synthetics (van Driel et al., 2015) at 25° epicentral distance for two events: A1 (top) and A6 (bottom), computed for source parameters reported in the SCARDEC (Vallée and Douet, 2016) and GCMT catalogs (Ekström et al., 2012), respectively. The corresponding focal mechanisms (beachballs) and focal depths are shown in the inset on the left. Dashed lines indicate predicted arrivals of the depth phases, pP and sS, respectively, of the two catalogs. For better visibility, the polarity of the A1 P-wave is reversed and the amplitudes of all waveforms are clipped.

All events are located in the vicinity of convergent plate boundaries. The regions include the Gulf of Mexico (A), Aleutians (B), North-Western Pacific (C), Himalaya (D), Australia (E), and South America (F), respectively. Careful assessment of seismic source parameters, including, hypocentral location, focal mechanism, and STF, is crucial for accurately modeling triplicated body waveforms (e.g., Stähler et al., 2012). Here, we rely on the SCARDEC catalog (Vallée and Douet, 2016), which provides estimates of source parameters based on teleseismic body wave recordings. We search this catalog for events within regional distances to broadband stations that are available through IRIS. The events are selected based on the following criteria:

1. availability of stations covering regional distances within a relatively narrow back azimuth bin ($<50°$) to reduce signature of lateral variations in mantle structure within a waveform section;
2. moment magnitudes of 5.8–7 and pulse-like mean STFs for improved signal-to-noise ratio (although larger events can have a more intricate STF that complicates waveforms); and
3. focal depths greater than 50 km for better separation of direct wave arrival and depth phase (i.e., pP and sS).

P- and S-waveform sections of events fulfilling these criteria are retained if no strong noise is seen in the data and uncertainties on source parameters are small. To verify that the latter is the case, we compare synthetic sections of Instaseis-waveforms (van Driel et al., 2015) computed for IASP91 and different source parameters, provided by SCARDEC and the Global Centroid Moment Tensor catalog (GCMT; Ekström et al., 2012). This is illustrated in Fig. 2B for waveform stacks of two exemplary events. Typically, effects can be seen around the depth phase due to differences in source depth estimates (cf. dashed lines vertical in Fig. 2B; event A1, S-wave >30 s; event A6, P-wave >20 s) and in relative amplitude variations because of differences in focal mechanisms (cf. Fig. 2B; event A1, P-wave; event A6, S-wave). We retain the waveform sections for which source uncertainties within the window of triplicated body wave arrivals are seen to be beneath the level of typical stack uncertainties cf. Fig. 2B; event A1, S-wave; event A6, P-wave.

The largest amount of data is available for the North American continent, including the Gulf of Mexico (region A) and Alaska (region B), through USArray, which consists of a set of permanent stations and an array of transportable seismometers with inter-station spacing of $\sim$70 km, that has been moved across the contiguous US from West to East in 2-year intervals and is currently located in Alaska. Here, we use recordings of earthquakes associated with the subduction of the Cocos plate under Central America to sample the MTZ beneath the Gulf of Mexico (region A). Region B uses an event that occurred underneath the Aleutian arc. Stations of the F-net (Full Range Seismograph Network of Japan; region C) are oriented in the direction of earthquakes that occurred in the Pacific and Philippine subduction trenches and therefore allow for triplication observations within a narrow back azimuth bin. Due to the seismotectonic setting in that region, nodal planes of many events are oriented towards the array and small variations in their exact orientation can have a large effect on waveform polarity. Since we wish to reduce sensitivity to source parameters (cf. Fig. 2B), we reject such events in that region. Similar issues are observed for region F (South America), as a result of which only one event is considered here. Region E (Australia) is also located in the vicinity of the Pacific subduction zone. However, accessible stations on the Australian continent are sparsely distributed, particularly in the Western part. Finally, we consider a single event in the Western part of the India-Eurasian collision zone (region D), which was recorded by the temporarily deployed (2003–2004) networks YA and XE in Eastern Tibet.

2.3. Data processing

For each event and station, we correct the seismic data for instrument response to obtain displacement. Traces are rotated to the vertical-radial-transverse (ZRT) system by using the back azimuth based on the SCARDEC-reported location. Our analysis uses the Z- and T-components to observe the P- and the horizontally polarized S-wave, respectively. We filter the waveforms using a Butterworth filter in the passbands 5–30 s for P- and 8–30 s for S-waves, respectively. Waveforms are trimmed to windows from −10 s to 30 s for P- and from −10 s to 45 s for S-waves, respectively, relative to the theoretical arrival time in IASP91. Each waveform is re-scaled to unity, using the highest absolute amplitude within a window of ±5 s relative to the first arrival as reference. We pick the first-arriving phase by means of cross-correlation with synthetics computed via the reflectivity method (Fuchs and Müller, 1971, cf. supplementary Figure S.2). This results in an estimate of differential travel time relative to IASP91, which is used to shift the entire waveform. This removes absolute travel time information, which is affected by source parameters and shallow structure. For events of regions A and B, we group data in distinct back azimuth bins and, to achieve maximum coverage, proceed with the bin that includes the transportable stations deployed at the time. Finally, we stack waveforms in epicentral distance bins of 1° width. Uncertainty of a stack built from n traces is assessed by bootstrap-analysis (Efron and Tibshirani, 1991). This method recombines n traces randomly picked from a distance bin to form 100 stacks, from which the standard deviation is taken as uncertainty estimate.

2.4. Model parametrization and forward problem

Following previous approaches that rely on the premise of a mantle built from segregated endmembers (basalt and harzburgite; cf. Xu et al., 2008; Khan et al., 2009; Munch et al., 2020; Bissig et al., 2021), we model mantle composition as either an equilibrium assemblage (EA) or mechanical mixture (MM) of the aforementioned lithologies. Similarly to Khan et al. (2009), we parametrize composition by varying basalt fraction (f_i) at discrete depth-nodes (Z_i) that represents the weight fraction of basalt in a basalt-harzburgite mixture (cf. orange lines and dots in Fig. 3). The resultant mineralogy, Φ, can be expressed for the two mixing models by:

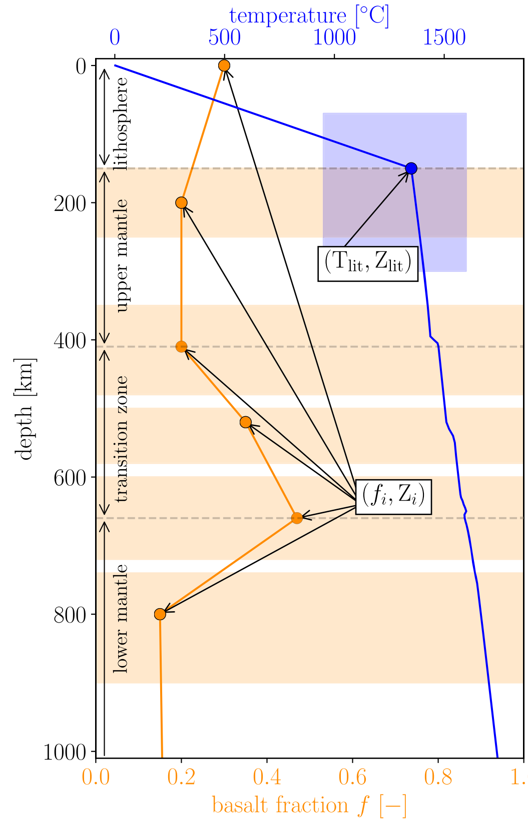

Fig. 3. Illustration of the model parametrization. Dots and colored regions indicate model parameters and prior ranges, respectively (cf. Table S.5): lithospheric thickness (Z_{lit}), temperature (T_{lit}), and basalt fraction (f_i) at variable depth nodes (Z_i). Composition at the core-mantle boundary (not shown) is an additional free parameter in the inversion. Solid lines show example profiles of basalt fraction (orange) and adiabatic geotherm (blue). Dashed gray lines depict the extent of the lithosphere, upper mantle, mantle transition zone, and lower mantle, respectively.

$$\mathrm{EA}: \ \Phi[f\mathbf{X}_{\mathrm{B}} + (1-f)\mathbf{X}_{\mathrm{H}}], \ \mathrm{MM}: \ f\Phi[\mathbf{X}_{\mathrm{B}}] + (1-f)\Phi[\mathbf{X}_{\mathrm{H}}], \quad (1)$$

where $\mathbf{X}_{\mathrm{B}}$ and $\mathbf{X}_{\mathrm{H}}$ are endmember compositions of basalt and harzburgite, respectively. Composition at intermediate depths is linearly interpolated from neighboring nodes. The chemical model considers the oxides of the major elements Na_2O, CaO, FeO, MgO, Al_2O_3, and SiO_2 (cf. Table S.3). In modeling temperature, we assume a conductive lithosphere, which is defined by thickness, Z_{lit}, basal temperature, T_{lit}, and fixed surface temperature, $T_{\mathrm{surf}} = 2°C$. Beneath, we consider an adiabatic mantle geotherm, which is self-consistently computed from the lithology at the bottom of the lithosphere. Temperature-related parameters are illustrated in Fig. 3 in blue. Finally, pressure is calculated from the surface through radial integration of the load. Crustal structure is modeled as a stack of layers with fixed seismic properties from IASP91. This is justified since we exclude from the inversion those parts of the waveform that are sensitive to crustal structure (cf. supplementary Figure S.3). We verified this by inverting the waveforms using the average station-side crust as reported in Crust1.0 (Laske et al., 2013) for three events, but observed no significant differences in the final results (cf. supplementary Figures S.22–S.24).

For a specific set of parameters, stable mineral phases are determined by Gibbs' free energy minimization and their physical properties via equation-of-state modeling through the software package Perple_X (Connolly, 2009) in combination with the thermodynamic formulation and data of Stixrude and Lithgow-Bertelloni (2005, 2011). Limitations of the thermodynamic model include the lack of data for minor phases, water, melt, and redox-effects. Furthermore, the equilibrium assumption is questionable at low temperatures

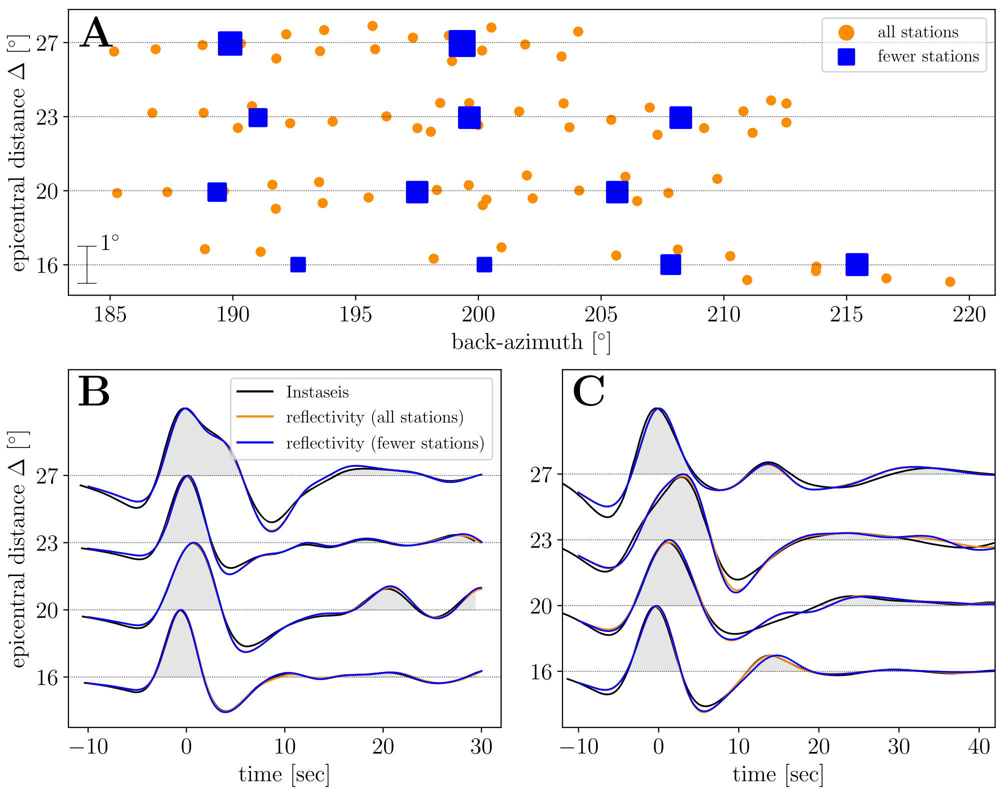

Fig. 4. Comparison of observed and synthetic stacking methods and synthetic waveforms. (**A**) In modeling synthetic stacks (here illustrated at epicentral distances of 16°, 20°, 23°, and 27° for event A5), we use a smaller set of stations indicated by the blue squares that mimic the epicentral distance and back azimuth distribution of the stations considered in building real stacks (indicated by the orange dots). The size of the blue squares indicates the number of observed traces within a particular distance-azimuth bin. (**B**) and (**C**) The corresponding waveform stacks (color-coded in panel (**B**) for P- and (**C**) for S-waves, respectively) are modeled by means of the reflectivity method (Fuchs and Müller, 1971) and benchmarked against Instaseis synthetics (van Driel et al., 2015, cf. supplementary Figure S.6 for the entire section).

(e.g., Wood and Holloway, 1984). That is why for temperatures below 500°C, we determine mineralogy at 500°C and evaluate physical properties at the temperature of interest. Uncertainties on density and elastic moduli were estimated to be around ∼0.5% and ∼1–2%, respectively (Connolly and Khan, 2016). For the purpose of modeling MM-based properties, we employ PHEMGP (Zunino et al., 2011) to extract physical properties from pre-computed tables. While bulk attenuation is held constant at $Q_\kappa = 57'823$ (Dziewonski and Anderson, 1981), we employ the laboratory-based extended Burgers model (Jackson and Faul, 2010), as implemented by Bagheri et al. (2019), to compute shear attenuation Q_μ. Parameters are listed in Table S.4.

In the inversion, we compare observed waveform stacks of a given event at discrete epicentral distances to their synthetic complements. The synthetic waveform stacks are built analogously to those constructed from real data using individual waveforms, which are computed with the reflectivity method (Fuchs and Müller, 1971) with source parameters provided by SCARDEC. In forming waveform stacks, we build upon an approach previously applied to receiver function modeling (Bissig et al., 2021). While a real stack is composed of individual seismograms recorded at many stations (orange dots in Fig. 4A), we compute synthetic waveforms at locations (blue squares) that mimic the observed epicentral distance and back azimuth distribution and weigh them by the number of observed traces within a particular distance-azimuth bin before stacking (indicated by the size of blue squares). This approach reduces the computational cost significantly by bypassing the need to model waveforms at all stations and is successfully benchmarked against Instaseis synthetics, as illustrated in Fig. 4B–C for event A5. To ensure accurate comparison between observed and synthetic waveform stacks, we adhere to our previous work (Munch et al., 2020; Bissig et al., 2021) and process real and synthetic waveforms similarly. Additional steps in waveform processing before summation include the convolution with the average SCARDEC-reported STF and the picking of the first-arriving wave by means of ray-tracing through the proposed seismic model. To ensure good alignment of synthetic and observed waveform stacks, we allow for timing corrections of ±2.5 s via cross-correlation.

Finally, in order to validate our 1-D modeling approach to computing synthetic seismograms, we benchmark our 1-D waveforms against 3-D full waveform synthetics. For this purpose, we employ the software package Salvus (Afanasiev et al., 2019) to compute full waveforms using the 3-D velocity models of Simmons et al. (2010) and Borgeaud et al. (2019) (cf. supplementary section S.2.2). Comparison of 1-D and 3-D synthetics shows that large velocity anomalies within the MTZ (dV_S up to ±5%) can impact our ability to model waveforms in detail.

2.5. Inverse problem

To solve the inverse problem, we use the probabilistic approach of Mosegaard and Tarantola (2002), where the solution is given in terms of:

$$p(\mathbf{m}|\mathbf{d}) \propto p(\mathbf{d}|\mathbf{m})p(\mathbf{m}), \qquad (2)$$

where $p(\mathbf{m}|\mathbf{d})$ is the posterior probability density of model, $\mathbf{m}$, given data, $\mathbf{d}$. It combines prior knowledge, $p(\mathbf{m})$, and the likelihood function, $p(\mathbf{d}|\mathbf{m})$. Here, the model vector is $\mathbf{m} = (T_{lit}, Z_{lit}, f_1, ..., f_n, Z_1, ..., Z_n)$. Observed data, $\mathbf{d}^{obs}$, correspond to waveform stacks for an event grouped by distance. P- and S-wave data are inverted jointly for events where both wave types are available. Observed stacks are compared to their synthetic counterparts, $\mathbf{d}^{\mathrm{syn}}$, by computing the misfit via:

$$\Phi_{i,j,k} = a\,\Phi^{\mathrm{CC}}_{i,j,k} + b\,\Phi^{\mathrm{L2}}_{i,j,k}, \tag{3}$$

for each available wave type i of the event (P/S), epicentral distance bin, j, and time window of interest, k, and where a and b are relative weights (0.75 and 0.25, respectively) that were chosen through trial-and-error to achieve optimal acceptance rates (to be detailed in the following). The first misfit function, $\Phi^{\mathrm{CC}}_{i,j,k}$, is based on a normalized correlation-coefficient (CC) measure, that has proven useful in inverting triplicated waveforms (Tao et al., 2017):

$$\Phi^{\mathrm{CC}}_{i,j,k} = 1 - \frac{\int \mathbf{d}^{\mathrm{syn}}_{i,j,k} \cdot \mathbf{d}^{\mathrm{obs}}_{i,j,k}\mathrm{dt}}{\sqrt{\int |\mathbf{d}^{\mathrm{syn}}_{i,j,k}|^2\mathrm{dt} \cdot \int |\mathbf{d}^{\mathrm{obs}}_{i,j,k}|^2\mathrm{dt}}} \tag{4}$$

The second misfit function, $\Phi^{\mathrm{L2}}_{i,j,k}$, follows a L_2-norm:

$$\Phi^{\mathrm{L2}}_{i,j,k} = \frac{1}{N}\sum_{n=1}^{N} \frac{||\mathbf{d}^{\mathrm{obs}}_n - \mathbf{d}^{\mathrm{syn}}_n||^2}{2\sigma_n^2}, \tag{5}$$

where σ_n is the uncertainty of the nth sample within a time window of length N and re-scaling by a factor of $1/N$ weights all windows equally. These windows are designed to exclude parts of the waveform stack that are affected either by source parameters or crustal structure. As mentioned earlier, distinct triplicated branches are more noticeable in S- than in P-wave sections. Therefore, misfit windows usually enclose separate phases in S-wave stacks, while for P-waves we invert data within a single window of ∼15–20 s length after the first-arriving P-wave. Finally, the likelihood function is calculated from separate misfit values via:

$$\mathrm{p}(\mathbf{d}|\mathbf{m}) = \prod_{i,j,k} \exp(-\Phi_{i,j,k}) \tag{6}$$

We apply a Metropolis-Hastings algorithm to sample the posterior distribution (e.g., Hastings, 1970). At each iteration n, a model, $\mathbf{m}^{n+1}$, is proposed and accepted with a probability of:

$$\min\left[1, \frac{\mathrm{p}(\mathbf{d}|\mathbf{m}^{n+1})}{\mathrm{p}(\mathbf{d}|\mathbf{m}^{n})}\right], \tag{7}$$

known as the Metropolis-rule. For each waveform stack available for the event under consideration, we compute the misfit value and evaluate the Metropolis-rule. Only if the change in misfit is accepted for every stack, the proposed model is retained. This is the cascaded Metropolis-rule (Mosegaard and Tarantola, 2002, see supplementary section S.3.1 for details).

Acceptance rates of the algorithm generally decrease with increasing number of stacks and wave types inverted. To achieve optimal acceptance rates of 30–50%, we

1. tune the step-sizes;
2. weigh Φ^{CC} more than Φ^{L2} via parameters a and b (cf. equation (3)), since runs using only Φ^{L2} were seen to result in very low acceptance rates. To still account for relative uncertainties between stacks, we kept Φ^{L2}, but decreased its importance with respect to Φ^{CC}, which tends to increase acceptance rates; and we
3. re-scale the uncertainties by a constant factor of 2 or 4 for all stacks of a data set in case of separate or joint P-/S-wave inversions, respectively, which is based on trial-and-error to achieve optimal acceptance rates without having to decrease step sizes too much.

For each event, we run two inversions using different modeling hypotheses (EA vs. MM mixing model). A first run (optimization stage; 16 chains run in parallel over 24 hours on a cluster) results in a set of initial models that serves as input for a second run (sampling stage; 16 chains run in parallel over 120 hours). This ultimately leads to 60’000–100’000 sampled models, with every 5th model (per chain) retained for analysis. Finally, the 10% worst fitting models are filtered out. Supplementary Figure S.13 illustrates the evolution of misfit for all first inversion runs. For the purposes of testing the inversion, we conducted synthetic tests. These are presented in supplementary section S.4.

3. Results

An exemplary datafit from the inversion of events A5 and A6 is shown in Fig. 5 for both mixing models, respectively. Corresponding plots for the other events are included in the supplementary material (Figures S.14–S.18). In Fig. 5, the P waveforms (panel A) are fit exceptionally well, while the datafit in the case of the S waveforms (panel B) is slightly degraded in comparison. This mainly reflects the generally more noisy character of S waveforms and potentially unmodeled structure related to lateral variations in properties. We observe a diminished datafit for some events. To investigate ways of improving datafit, we have re-inverted P-wave stacks of event A5 in a number of ways (cf. supplementary Figure S.25): 1) inversion of data subsets covering smaller epicentral distances or back azimuth ranges; and 2) allowing for positive and negative deviations from the adiabat. None of these approaches appeared to result in a substantial improvement of the datafit and may suggest unmodeled structure, possibly related to the presence of 3-D structure.

To study the depth sensitivity and resolution of the sampled seismic velocity and compositional models quantitatively, we evaluate Shannon’s measure of information content (see supplementary section S.3.2). The resulting profiles of information content for velocity and composition are shown in Fig. 6A and B, respectively, and are compared to the depth distribution at which the triplicated waves, that are observed in our data set, turn (Fig. 6C). We see that the information content is largest at depths that are 1) sampled most extensively (∼600–800 km) and 2) where, because of near-horizontal propagation close to the turning point, resolution is highest. Associated with a decrease in the number of turning points is a reduction in information content at mid-MTZ depths (∼450-550 km), which is less pronounced for seismic velocities than composition. This results from temperature (cf. supplementary Figure S.4) counterbalancing the diminished compositional resolution and therefore accounting for a part of the gain in information content in the mid-MTZ velocity structure. Despite the smaller number of turning points in the depth range 350–450 km, the mantle appears well-resolved. While counterintuitive, this results from the thermally-sensitive nature of the 410 (e.g., Khan et al., 2013), which is connected to the deeper densely-sampled MTZ through the adiabatic geotherm.

In the following, we focus on comparing our results by studying trends in thermochemical structure and degree of equilibration common to all subduction zones rather than concentrating on individual locations. To investigate the differences in thermochemical structure associated with the mixing models employed, we compare EA- and MM-based mean values of inverted parameters for all events by measuring Pearson’s correlation coefficient (χ; see supplementary section S.3.3). To facilitate comparison of thermal models, we rely on potential temperature, $\mathrm{T_{pot}}$, (McKenzie and Bickle, 1988). Fig. 7A shows the correlation between potential temperatures from the two mixing models, that are seen to correlate relatively well ($\chi = 0.701$), although MM tends to cover a larger temperature range

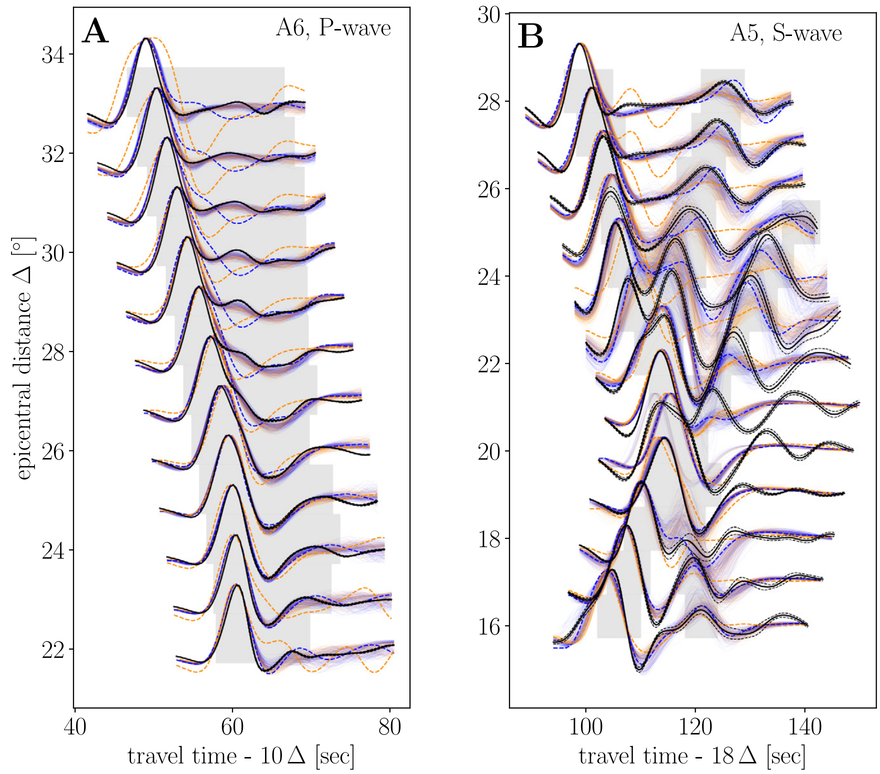

Fig. 5. Exemplary P- and S-wave datafit for event A6 (**A**) and A5 (**B**), respectively. Observed waveform stacks are displayed as black solid lines and their uncertainties with black dashed lines. A random selection of 150 synthetic stacks sampled in the inversion are shown in blue and orange in the case of equilibrium assemblage (EA) and mechanical mixture (MM) inversions, respectively. Synthetic waveform stacks based on initial models are shown as colored dashed lines. Windows used for misfit computation are shaded in gray. P- and S-waveform fits for the other events are shown in Figures S.14–S.18.

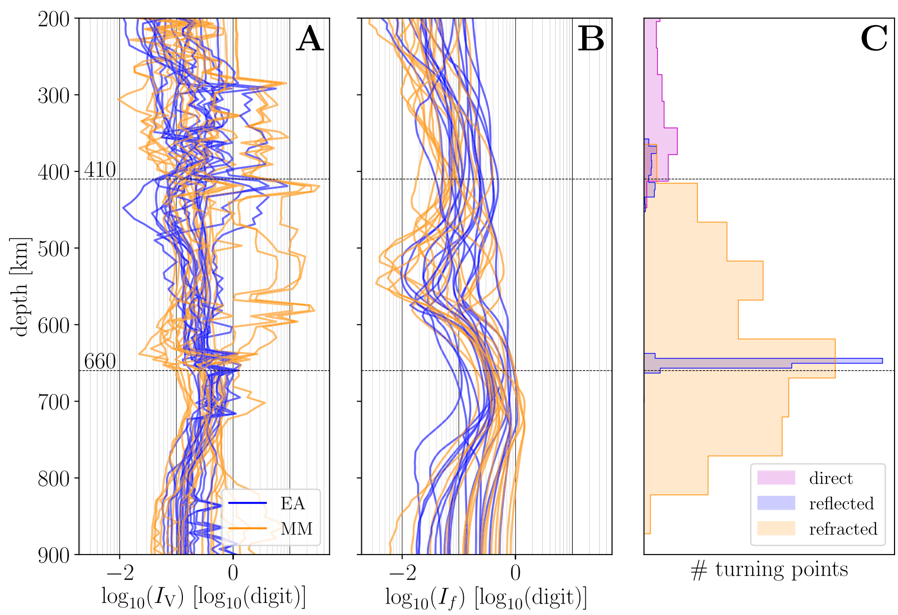

Fig. 6. Shannon's information content evaluated for seismic velocities I_V (**A**) and basalt fraction I_f (**B**). Note that in (**A**) information content is based on both P- and S-wave velocity. (**C**) illustrates the distribution of turning points with depth, which is a measure of the sensitivity, as seen by the entire data set. Computation of turning point depth for each event is based on a random selection of 150 models from the posterior. Information content is computed relative to the respective prior distributions (cf. Fig. 3 and supplementary Table S.5). For details see main text and supplementary section S.3.2.

(∼1000–1500°C) relative to EA (∼1100–1450°C). Potential temperature values for most events average around 1200°C for either mixing model.

An indirect measure of temperature is MTZ thickness, ΔZ_{MTZ}, which reflects the combined behavior of the 410- and 660-topography in the presence of lateral thermal variations. Since the absolute value of the Clapeyron slope of the 410 is larger than the 660, MTZ thickness is mainly dominated by the 410 (e.g., Bissig et al., 2021). Because the Clapeyron slope of the 410 is positive (Katsura et al., 2010), lower/higher temperatures move the 410 to shallower/greater depth and hence lead to an overall thicker/thinner MTZ, respectively. In Fig. 7B, we show the average

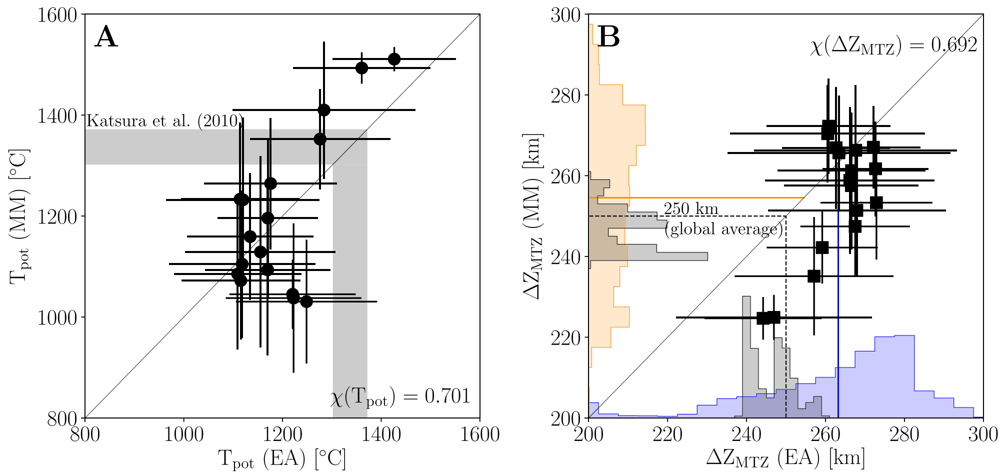

Fig. 7. Correlation between equilibrium assemblage (EA) and mechanical mixture (MM) models of (**A**) mean potential temperature (T_{pot}) and (**B**) mantle transition zone (MTZ) thickness (ΔZ_{MTZ}) for all events. Uncertainty estimates (standard deviations) are indicated by error bars. Pearson's correlation coefficient is denoted by χ. The laboratory-based potential temperature of Katsura et al. (2010) is indicated by the gray shaded area in (**A**). For comparison, the global average MTZ thickness of 250 km is also plotted in (**B**) (black dashed lines) alongside the marginal distributions and mean values (solid lines) of MTZ thickness obtained here (blue and orange) and by Tian et al. (2020) from analysis of SS-precursors (gray; see main text for details).

MTZ thickness estimated from the sampled seismic velocity profiles, which shows a variability of ∼240–280 km for most events.

Estimates of basalt fraction at different depths from EA and MM inversions are compared in Fig. 8A. A robust trend from compositions enriched in basalt at 500 km (on average 0.45/0.59 for EA/MM, respectively) to a more pyrolitic chemistry (0.26/0.20 for EA/MM, respectively) at 700 km is well-defined for both mixing models ($\chi = 0.770$). However, for a given depth, correlations between EA and MM decrease (not shown) and reflect subtle compositional differences between mixing models. MM models tend to larger compositional gradients, i.e., enrichments/depletions within/underneath the MTZ, respectively, that are more pronounced relative to EA. This is explained by the reduced sensitivity of MM models to composition within the MTZ (Xu et al., 2008, cf. Figure S.4), which leads to larger compositional gradients to achieve the variations in seismic properties required by the data. Moreover, compositional variations are larger within the MTZ, in line with the decreased sensitivity discussed above (cf. Fig. 6B). Hence, compositional inferences within are less certain than underneath the MTZ. This is illustrated with the mean profiles of basalt fraction shown in Fig. 8B (color-coded by mixing model), where the width and transparency of individual profiles are determined by Shannon's information content at the respective depth. A loss in resolution at mid-MTZ depths, as illustrated by fading lines, is noticeable for several events. Note that the general trend of a more fertile MTZ relative to a depleted topmost lower mantle is confirmed by the well-resolved events in region A and possibly C, D, and E and is in qualitative agreement with other seismic studies (e.g., Cammarano et al., 2009; Wu et al., 2019).

Despite differences in thermochemical models, we expect the similar datafit of mixing models (Fig. 5) to result from similarity in seismic velocity models. This is considered in more detail in Fig. 9, where we compare mean P-wave velocities (V_P) and standard deviations for EA and MM inversions. Because the majority of inverted waveforms are P-wave recordings, we focus on discussing P-wave velocities, although similar conclusions are drawn from a comparison of S-wave velocities. Fig. 9A compares mean P-wave velocities at depths of 500, 600, and 700 km. There is a strong correlation between EA and MM estimates ($\chi = 0.985$), which explains the similar datafit of both mixing models. Absolute seismic velocities within the MTZ from either EA or MM inversions (Fig. 9A) are of similar magnitude when compared to 1-D seismic models IASP91 (Kennett and Engdahl, 1991) and PREM (Dziewonski and Anderson, 1981). While the average velocity structure of EA- and MM-based models generally correlate well over the entire data set, differences in velocity structure between mixing models become clearer for individual events. Sampled seismic profiles are compared to regional models (cf. Table S.6) in Figure S.19 and for those models, where significant differences are extant, we also computed waveform fits (Figure S.14–S.18). The comparison shows that in all cases our model ensemble results in an improved waveform fit.

To investigate the cause of the velocity variations, Fig. 9 shows the correlation between P-wave velocity and potential temperature (panel B) and P-wave velocity and composition (panel C) for EA-inversions, respectively. We see that P-wave velocity correlates well with temperature within the MTZ, resulting in correlation coefficients of $\chi = -0.819$ at 500 km and $\chi = -0.896$ at 600 km, respectively, as opposed to $\chi = -0.198$ and $\chi = -0.070$ for composition. Compositional effects become more important in explaining seismic velocity below the 660, where the compositional and thermal correlation coefficients of $\chi = -0.676$ and $\chi = -0.554$, respectively, are closer. Not surprisingly, this agrees well with the gain in compositional information content below the MTZ (cf. Fig. 6B). This behavior is similar in the case of MM inversions (cf. supplementary Figure S.20) and emphasizes the importance of considering compositional variations when interpreting seismic velocities as demonstrated in our previous work (e.g., Khan et al., 2009; Munch et al., 2020; Bissig et al., 2021).

We employ the Bayes' factor (see supplementary section S.3.4), which provides a measure of the relative importance of one hypothesis over another on the basis of data and prior information. The hypotheses that we wish to investigate are: the mantle is fully-equilibrated with depth (hypothesis $\mathcal{H}_i$) and the mantle is made up of a mechanical mixture with depth (hypothesis $\mathcal{H}_j$). If the Bayes' factor, $\mathcal{B}_{ij} > 1$ then $\mathcal{H}_i$ is favored, whereas if $\mathcal{B}_{ij} < 1$ then $\mathcal{H}_j$ is favored. The results of this analysis are illustrated in Fig. 10, which shows how $\mathcal{B}_{ij}$ varies with depth (here indicated by the depth at which direct, reflected, and refracted waves turn in the mantle). What we observe is that while there are depths for which $\mathcal{B}_{ij}$ is both >1 and <1, the depth- and event-integrated (histogram on the ordinate) marginal distribution shows that $\mathcal{B}_{ij} > 1$. The former observation is in line with the intermittent nature of material flux through the mantle transition zone whereas the latter observation indicates that on average the mantle is better described by an equilibrum assemblage than a mechanical mixture (at least across most of the subduction settings studied here).

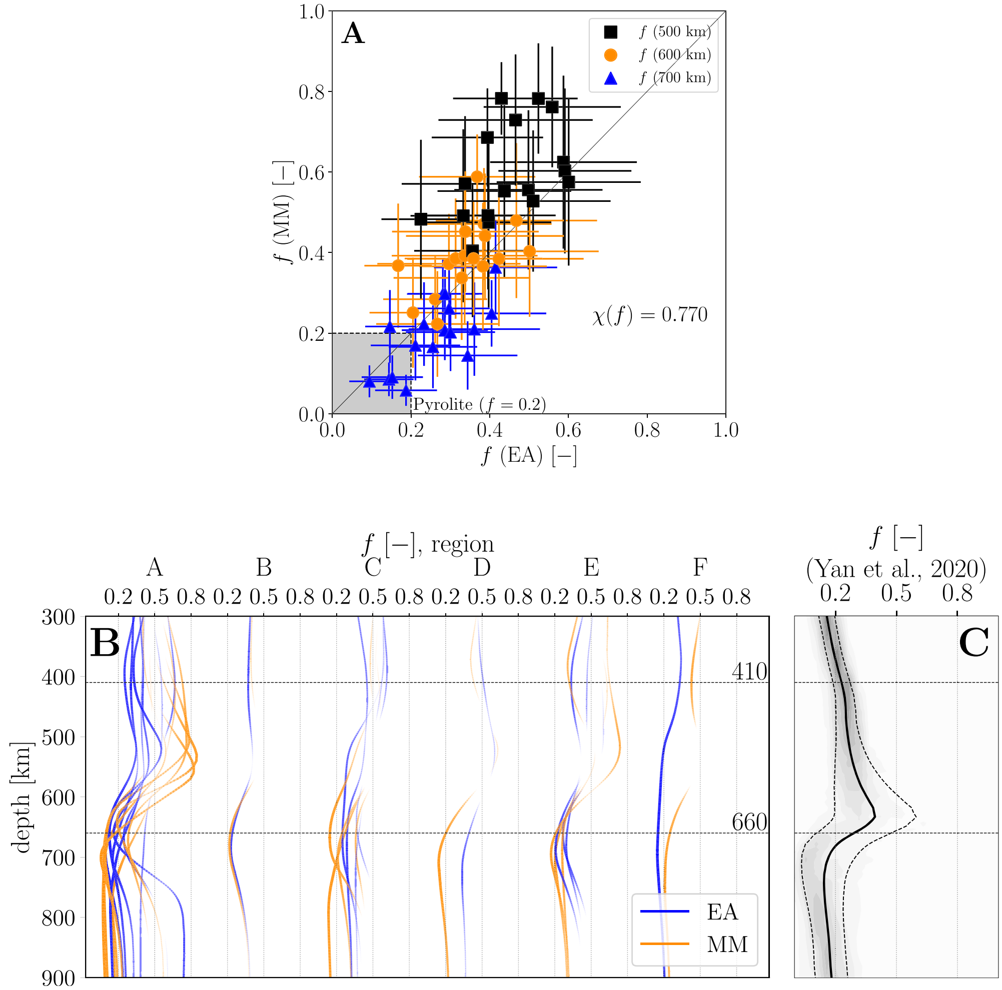

Fig. 8. Correlation between equilibrium assemblage (EA) and mechanical mixture (MM) models of basalt fraction (f) at different depths in the mantle transition zone (**A**) for all events. Uncertainty estimates (standard deviation) are indicated by error bars. Correlation is quantified by Pearson's correlation coefficient (χ). The gray shaded area represents the harzburgite-rich side of the pyrolitic composition (indicated by a dashed line). (**B**) EA- and MM-based mean profiles of basalt fraction, respectively, sorted by region (cf. Fig. 2). The width and transparency of each line represents Shannon's information content with depth, i.e., fading lines indicate less well-resolved regions. (**C**) modeled basalt fraction profiles from Yan et al. (2020) obtained from numerical convection simulations (see main text for details).

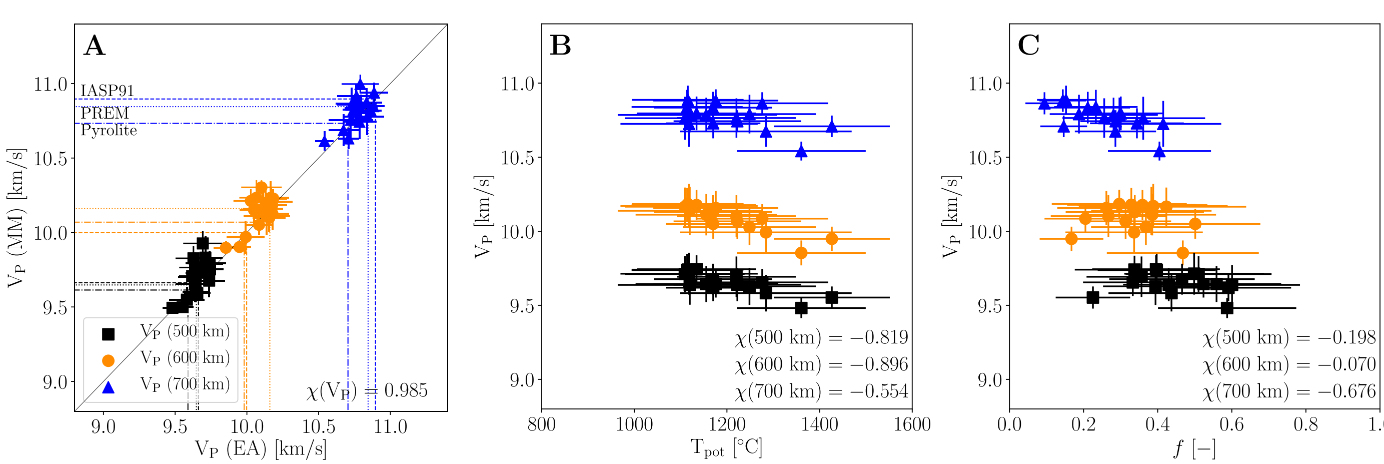

Fig. 9. Comparison of P-wave velocity models. (**A**) Correlation of mean EA- and MM-based P-wave velocities (V_P) at various depths in the mantle transition zone (MTZ) for all events. For comparison, we show V_P at the same depths for the seismic reference models IASP91 (Kennett and Engdahl, 1991), PREM (Dziewonski and Anderson, 1981), and a pyrolitic mantle model with potential temperature of ∼1350°C. (**B**) and (**C**) correlation of EA-based V_P with potential temperature (T_{pot}); (**B**) and basalt fraction (f); (**C**) at different depths within the MTZ. Error bars indicate standard deviations based on all sampled models and Pearson's correlation coefficient is indicated by χ.

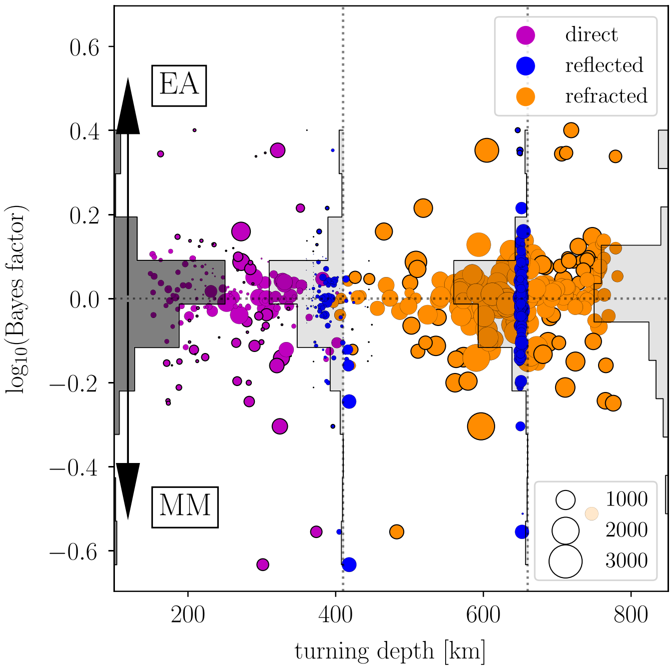

Fig. 10. Radial variation in mantle mixing state. Bayes' factor as a function of depth at which the direct, reflected, and refracted waves turn (turning depth), respectively. The size of the dots denote the number of turning points observed at a particular depth. The histogram on the left shows the depth- and event-integrated distribution of the Bayes' factor. Marginal histograms of Bayes' factor for the upper mantle (< 410 km), the mantle transition zone (410 − 660 km), and the lower mantle (> 660 km) are shown in light gray.

4. Discussion

The potential temperature estimates found here are lower than earlier global estimates (e.g., McKenzie and Bickle, 1988; Katsura et al., 2010; Munch et al., 2020), but likely reflect the inclusion of subduction zone settings, where, because of the presence of ancient slabs, lateral temperature variations of up to 500°C can be reached (Tan et al., 2002). As evidenced by our results (cf. Fig. 7A), we see no systematic differences in temperature values between mixing models, in line with Munch et al. (2020). Because of the lower temperatures found here, MTZ thickness is greater than the global average of ∼240–250 km (e.g., Andrews and Deuss, 2008; Tauzin et al., 2008; Munch et al., 2020). Similarly, Tauzin et al. (2008) found, from analysis of P-to-s converted waves, that the MTZ underneath 2/3 of the stations associated with a subduction setting is up to 40 km thicker than average. Their estimate of the associated lateral temperature variations for these regions (−100 to −300°C) is in agreement with the lower-than-average temperatures found here.

To take the comparison further, we consider the recent global MTZ thickness model of Tian et al. (2020) based on SS-precursor travel times. For each station-event pair in our data set, we interpolate the model of Tian et al. (2020) to the turning point location of the wave traveling from the event to the station considered. The distribution of all interpolated MTZ thickness values associated with an event are compared to our corresponding distributions in Fig. 7B. Overall, the MTZ thickness values of Tian et al. (2020) are closer to 250 km and have smaller variances than our estimates, resulting in a 17.0 km and 8.4 km thinner MTZ on average for EA and MM, respectively, compared to our results. These differences arise from a number of issues. Firstly, while SS-precursors are more sensitive to discontinuity depth than triplicated waves, the period range (15–75 s) employed by Tian et al. (2020) averages topography over larger areas. Secondly, the time-to-depth conversion needed for mapping SS-precursor travel times to discontinuity depth is sensitive to the background model employed. Thirdly, due to a decrease in turning point density (cf. Fig. 6C), our data set is overall less sensitive to the depth of the 410, which results in larger variances in MTZ thickness. Combining the sensitivities of precursors and triplicated waveforms in a single inversion could help disentangle discrepancies in MTZ thickness estimates.

The simplest model of mantle composition is that of an equilibrated, homogeneous pyrolite (e.g., Ringwood, 1975), which is capable of explaining mid-ocean ridge basalt compositions (e.g., McKenzie and Bickle, 1988) and the radial seismic velocity structure of the mantle to first order (e.g., Weidner, 1985; Jackson and Rigden, 1998). Yet, there are many indications that deviations from the pyrolitic model are required to account for the seismic properties of the mantle (e.g., Agee, 1993; Cammarano et al., 2009; Khan et al., 2009). Clearly, our basalt fraction profiles (blue and yellow lines in Fig. 8B) require additional compositional complexities beyond pyrolite to explain the triplicated waveforms.

The transition from more equilibrated to mechanically-mixed portions of the mantle is primarily governed by the relative timescales of mantle stirring and diffusion coefficients, which would appear to favor MM over EA (e.g., Hofmann and Hart, 1978; Allègre and Turcotte, 1986). Yet, more equilibrated mantle regions should exist, where diffusion is more efficient relative to mantle convection, as proposed for the topmost MTZ based on measurements of Fe-Mg diffusion coefficients of olivine and its high-pressure polymorphs that increase by 6–7 orders of magnitude at the 410 (Holzapfel et al., 2009). Based on our results (Fig. 10), we do not see any signs for a transition from more equilibrated mantle portions to deeper regions where mechanical mixing dominates on average. Nevertheless, subtle preferences for either mixing model are present that imply a heterogeneous pattern of equilibration across the mantle, while, on average, equilibrium assemblage appears to be favored. This implies that mixing is more efficient close to subduction zones, which could be related to higher diffusion coefficients seen in fluid-rich mantle (Hofmann and Hart, 1978), in line with the dehydration of subducted peridotite at MTZ-depths (e.g., Hirschmann, 2006). This fits well into the overall picture of a heterogeneous mantle, where sub-cratonic regions (Munch et al., 2020) are less and subduction zones regions more equilibrated.

Although our results indicate a slight preference for an equilibrated mantle, other arguments that favor MM over EA have been put forward, including major and trace element geochemistry (e.g., White, 2010) and studies of seismic scatterers (e.g., Kaneshima, 2016). Here, we compare MM-based compositional models to outcomes from a recent study by Yan et al. (2020), who employed global-scale 2-D thermochemical convection models to simulate the evolution and distribution of mantle heterogeneities, following an earlier study by Ballmer et al. (2015). In Fig. 8C, we show the probability contours, mean, and standard deviation of the compositional profiles by Yan et al. (2020), which are extracted at every 8.4° from the mesh and cover the last ∼4.0–4.5 Gyr of the reference simulation. The profiles are in agreement with earlier suggestions (e.g., Irifune and Ringwood, 1993), that the MTZ is enriched in basalt as opposed to a more harzburgitic reservoir below the 660, which had been attributed to a density-crossover in the harzburgitic and basaltic lithologies at the 660. Yan et al. (2020) found this type of profile to be robust over a wide parameter range, although within <1000 km of subduction zones, profiles can be more complex. While some profiles appear to be less well-resolved in the MTZ (Figure 8B), the combination of Figures 8A and 8B nevertheless suggests a trend from more fertile (at mid-MTZ depths) to more depleted compositions (within the deeper MTZ). For the comparison with Yan et al. (2020), we focus on the well-resolved profiles (e.g., region A).

We find maximum basalt fractions of ∼0.5–0.8 at ∼500–600 km depth as opposed to ∼0.2–0.6 at 620–660 km depth by Yan et al. (2020). These discrepancies in absolute values and depth ranges can be explained by a series of factors:

1. The choice of parameters in the geodynamic simulations can alter absolute basalt fractions above the 660. While viscosity affects basalt fraction by a few percent, variable friction coefficients that govern the style of plate-tectonics and initial compositions are capable of varying mean basalt fraction above the 660 in the range ∼0.2–0.6.
2. The deviations in absolute values and depth of enrichment might be attributed to the model parametrization employed here, that is, choice of adiabatic geotherm and prior range of compositional node depths. The former assumption is challenged by numerical convection simulations and seismic studies, that indicate that the geotherm is more likely to be both sub- (e.g., Sinha and Butler, 2007) and super-adiabatic (e.g., Khan et al., 2009). However, re-inversion of three events (A1, A4, and A6) using (1) non-adiabatic geotherms with positive thermal gradients, and (2) shifting the prior bounds on node depth by +50 km, results in overall similar compositional profiles.
3. The effect of low temperatures on seismic velocities is opposite to that of high basalt fractions (cf. supplementary Figure S.4) and could lead to a potential overestimation of compositional enrichments had we underestimated temperatures. Assuming a difference of about 10 km in MTZ thickness relative to the model of Tian et al. (2020) to arise from too low temperatures would correspond to a correction of our temperature estimates by ∼100°C. Supplementary Figure S.5 illustrates that at 550 km depth, a decrease in basalt fraction by ∼0.2 would be needed to absorb such an increase in temperature in order to keep seismic velocities constant.
4. High mid-MTZ basalt fractions observed in region A can represent an actual regional geodynamic feature, which is not visible in Fig. 8C due to spatial and temporal averaging of the geodynamic profiles. While plumes and stagnant slabs are the primary mechanisms for basalt enrichments in the MTZ, slabs that penetrate the 660 can remove basaltic material from the MTZ through entrainment (Ballmer et al., 2015; Yan et al., 2020). For region A, both recent and ancient subduction of the Cocos and Farallon slabs (e.g., Sigloch, 2011) could affect mantle composition. The large enrichments suggest that segregation and accumulation of basalt are dominant over removal through entrainment. This might point to diminished mantle viscosity and stiffer oceanic crust, that favors the segregation of basalt from harzburgite in a downgoing slab (Karato, 1997).

5. Conclusions and outlook

In this study, we investigated the physical and chemical structure of the mantle transition zone (MTZ) using a carefully selected set of triplicated P- and S-waveforms at a number of locations across the globe with a view to providing insights into mantle dynamics through its imprint on the MTZ. This is made possible through the implementation of a methodology that interfaces geophysical inversion with self-consistent calculations of mineral phase equilibria and physical properties. Our results are compatible with a compositional trend from more fertile lithologies at mid-MTZ depths to more pyrolitic compositions below the MTZ, in overall agreement with the segregation and accumulation of basalt within the MTZ as observed in numerical convection simulations. However, we only examined a few subduction zones among which region A and possibly C, D, and E show evidence for basalt enrichment. Other localities lack the resolution to resolve the basalt fraction at mid-MTZ depth. Whether a fertile MTZ is common to all subduction zones and other tectonic settings needs to be investigated further. Despite small variations in datafit across the various locations considered here, we find that some regions are better fit using an equilibrated mantle, whereas others fare better when relying on a mechanically-mixed mantle, but that, on average, an equilibrium assemblage appears to be, from a statistical perspective, more probable.

While the proposed method delineates a means for quantitatively studying structure and constitution of the MTZ (and that of the mantle generally) using regional waveforms, we suffer from a number of limitations. Firstly, the strict data selection criteria employed here limit the number of useful events. This could be relaxed if we were to include source parameters in the inversion (e.g., Stähler et al., 2012), which would allow us to extend our analysis to shallow events and thus to tectonic settings other than subduction zones. Secondly, 3-D full waveform inversion (e.g., Borgeaud et al., 2019), in tandem with source inversion, would allow for exploiting absolute travel time information contained in triplicated waveforms and possibly improved waveform fits. Finally, the information content of the data set can be increased by including additional data types that provide sensitivity to upper mantle structure as well as discontinuity depth, amplitude, and sharpness (e.g., surface wave dispersion, converted waves, and precursors). This will lead to further improvement in our understanding of the nature of the MTZ at inter-regional scales.

CRediT authorship contribution statement

Felix Bissig: Conceptualization, Formal analysis, Investigation, Methodology, Software, Validation, Visualization, Writing – original draft, Writing – review & editing. **Amir Khan:** Conceptualization, Formal analysis, Funding acquisition, Investigation, Methodology, Software, Supervision, Validation, Visualization, Writing – review & editing. **Domenico Giardini:** Funding acquisition, Supervision.

Declaration of competing interest

The authors declare that they have no known competing financial interests or personal relationships that could have appeared to influence the work reported in this paper.

Acknowledgements

We are grateful to two anonymous reviewers for their constructive comments that led to an improved manuscript and the editor, Hans Thybo, for editorial handling. This study is supported by a grant from the Swiss Federal Institute of Technology (project number ETH-05 17-1). Seismic data were downloaded via ObspyDMT (doi: 10.5281/zenodo.801778) from IRIS and processed using Obspy (doi: 10.5281/zenodo.3921997). IRIS Data Services are funded through the Seismological Facilities for the Advancement of Geoscience (SAGE) Award of the National Science Foundation under Cooperative Support Agreement EAR-1851048. F-net data are provided by the National Research Institute for Earth Science and Disaster Resilience (NIED) and were downloaded from www.fnet.bosai.go.jp/. SSN data was obtained by the Servicio Sismológico Nacional México (www.ssn.unam.mx), station maintenance, data acquisition and distribution is thanks to its personnel. SCARDEC source parameters were obtained from scardec.projects.sismo.ipgp.fr/. Perple_X is available on www.perplex.ethz.ch and PHEMGP on github.com/inverseproblem/Phemgp. We thank D. Tian and J. Yan for sharing their models with us. Computations were performed on the clusters Euler (ETH) and Piz Daint (CSCS). Computations on Piz Daint were supported by the Swiss National Supercomputing Centre (CSCS) under Project ID s922.

Appendix A. Supplementary material

Supplementary material related to this article can be found online at https://doi.org/10.1016/j.epsl.2022.117387.

References

Afanasiev, M., Boehm, C., van Driel, M., Krischer, L., Rietmann, M., May, D.A., Knepley, M.G., Fichtner, A., 2019. Modular and flexible spectral-element waveform modelling in two and three dimensions. Geophys. J. Int. 216, 1675–1692. https://doi.org/10.1093/gji/ggy469.

Agee, C.B., 1993. Petrology of the mantle transition zone. Annu. Rev. Earth Planet. Sci. 21, 19–41. https://doi.org/10.1146/annurev.ea.21.050193.000315.

Allègre, C.J., Turcotte, D.L., 1986. Implications of a two-component marble-cake mantle. Nature 323, 123–127.

Andrews, J., Deuss, A., 2008. Detailed nature of the 660 km region of the mantle from global receiver function data. J. Geophys. Res. 113. https://doi.org/10.1029/2007JB005111.

Bagheri, A., Khan, A., Al-Attar, D., Crawford, O., Giardini, D., 2019. Tidal response of Mars constrained from laboratory-based viscoelastic dissipation models and geophysical data. J. Geophys. Res., Planets 124. https://doi.org/10.1029/2019JE006015.

Ballmer, M.D., Schmerr, N.C., Nakagawa, T., Ritsema, J., 2015. Compositional mantle layering revealed by slab stagnation at ∼1000-km depth. Sci. Adv. 1. https://doi.org/10.1126/sciadv.1500815.

Bissig, F., Khan, A., Tauzin, B., Sossi, P.A., Munch, F.D., Giardini, D., 2021. Multifrequency inversion of Ps and Sp receiver functions: methodology and application to USArray data. J. Geophys. Res., Solid Earth 126. https://doi.org/10.1029/2020JB020350.

Borgeaud, A.F.E., Kawai, K., Geller, R.J., 2019. Three-dimensional S velocity structure of the mantle transition zone beneath Central America and the Gulf of Mexico inferred using waveform inversion. J. Geophys. Res., Solid Earth 124, 9664–9681. https://doi.org/10.1029/2018JB016924.

Cammarano, F., Romanowicz, B., Stixrude, L., Lithgow-Bertelloni, C., 2009. Inferring the thermochemical structure of the upper mantle from seismic data. Geophys. J. Int. 179, 1169–1185. https://doi.org/10.1111/j.1365-246X.2009.04338.x.

Connolly, J.A.D., 2009. The geodynamic equation of state: what and how. Geochem. Geophys. Geosyst. 10, 1–19. https://doi.org/10.1029/2009GC002540.

Connolly, J.A.D., Khan, A., 2016. Uncertainty of mantle geophysical properties computed from phase equilibrium models. Geophys. Res. Lett. 43, 1–9. https://doi.org/10.1002/2016GL068239.

Dziewonski, A.M., Anderson, D.L., 1981. Preliminary reference Earth model. Phys. Earth Planet. Inter. 25, 297–356. https://doi.org/10.1016/0031-9201(81)90046-7.

Efron, B., Tibshirani, R., 1991. Statistical data analysis in the computer age. Science 253, 390–395. https://doi.org/10.1126/science.253.5018.390.

Ekström, G., Nettles, M., Dziewonski, A.M., 2012. The global CMT project 2004-2010: centroid-moment tensors for 13,017 earthquakes. Phys. Earth Planet. Inter. 200–201, 1–9. https://doi.org/10.1016/j.pepi.2012.04.002.

Fuchs, K., Müller, G., 1971. Computation of synthetic seismograms with the reflectivity method and comparison with observations. Geophys. J. Int. 23, 417–433. https://doi.org/10.1111/j.1365-246X.1971.tb01834.x.

Grand, S.P., 2002. Mantle shear-wave tomography and the fate of subducted slabs. Philos. Trans. R. Soc. A 360, 2475–2491. https://doi.org/10.1098/rsta.2002.1077.

Hastings, W.K., 1970. Monte Carlo sampling methods using Markov chains and their applications. Biometrika 57, 97–109. https://doi.org/10.2307/2334940.

Helffrich, G., 2000. Topography of the transition zone discontinuities. Rev. Geophys. 38, 141–158. https://doi.org/10.1029/1999RG000060.

Hirschmann, M.M., 2006. Water, melting, and the deep Earth H_2O cycle. Annu. Rev. Earth Planet. Sci. 34, 629–653. https://doi.org/10.1146/annurev.earth.34.031405.125211.

Hofmann, A.W., Hart, S.R., 1978. An assessment of local and regional isotopic equilibrium in the mantle. Earth Planet. Sci. Lett. 38, 44–62. https://doi.org/10.1016/0012-821X(78)90125-5.

Holzapfel, C., Chakraborty, S., Rubie, D.C., Frost, D.J., 2009. Fe-Mg interdiffusion in wadsleyite: the role of pressure, temperature and composition and the magnitude of jump in diffusion rates at the 410 km discontinuity. Phys. Earth Planet. Inter. 172, 28–33. https://doi.org/10.1016/j.pepi.2008.09.005.

Irifune, T., Ringwood, A.E., 1993. Phase transformations in subducted oceanic crust and buoyancy relationships at depths of 600-800 km in the mantle. Earth Planet. Sci. Lett. 117, 101–110. https://doi.org/10.1016/0012-821X(93)90120-X.

Ishii, M., Tromp, J., 1999. Normal-mode and free-air gravity constraints on lateral variations in velocity and density of Earth's mantle. Science 285, 1231–1236. https://doi.org/10.1126/science.285.5431.1231.

Jackson, I., Faul, U.H., 2010. Grainsize-sensitive viscoelastic relaxation in olivine: towards a robust laboratory-based model for seismological application. Phys. Earth Planet. Inter. 183, 151–163. https://doi.org/10.1016/j.pepi.2010.09.005.

Jackson, J., Rigden, S.M., 1998. Composition and temperature of the Earth's mantle: seismological models interpreted through experimental studies of Earth material. In: Jackson, I. (Ed.), The Earth's Mantle: Composition, Structure and Evolution. Cambridge Univ. Press, New York.

Jackson, M.G., Dasgupta, R., 2008. Compositions of HIMU, EM1, and EM2 from global trends between radiogenic isotopes and major elements in ocean island basalts. Earth Planet. Sci. Lett. 276, 175–186. https://doi.org/10.1016/j.epsl.2008.09.023.

Kaneshima, S., 2016. Seismic scatterers in the mid-lower mantle. Phys. Earth Planet. Inter. 257, 105–114. https://doi.org/10.1016/j.pepi.2016.05.004.

Karato, S., 1997. On the separation of crustal component from subducted oceanic lithosphere near the 660 km discontinuity. Phys. Earth Planet. Inter. 99, 103–111. https://doi.org/10.1016/S0031-9201(96)03198-6.

Katsura, T., Yoneda, A., Yamazaki, D., Yoshino, E.I., 2010. Adiabatic temperature profile in the mantle. Phys. Earth Planet. Inter. 183, 212–218. https://doi.org/10.1016/j.pepi.2010.07.001.

Kennett, B.L.N., Engdahl, E.R., 1991. Traveltimes for global earthquake location and phase identification. Geophys. J. Int. 105, 429–465. https://doi.org/10.1111/j.1365-246X.1991.tb06724.x.

Khan, A., Boschi, L., Connolly, J.A.D., 2009. On mantle chemical and thermal heterogeneities and anisotropy as mapped by inversion of global surface wave data. J. Geophys. Res. 114, 1–21. https://doi.org/10.1029/2009JB006399.

Khan, A., Zunino, A., Deschamps, F., 2013. Upper mantle compositional variations and discontinuity topography imaged beneath Australia from Bayesian inversion of surface-wave phase velocities and thermochemical modeling. J. Geophys. Res. 118. https://doi.org/10.1002/jgrb.50304.

Laske, G., Masters, G., Ma, Z., Pasyanos, M., 2013. Update on CRUST1.0 - A 1-degree global model of Earth's crust. Geophys. Res. Abstr. 15. Abstract EGU2013-2658.

Li, J., Chen, M., Ning, J., Bao, T., Maguire, R., Flanagan, M.P., Zhou, T., 2022. Constraining the 410-km discontinuity and slab structure in the Kuril subduction zone with triplication waveforms. Geophys. J. Int. 228, 729–743. https://doirig/10.1093/gji/ggab361.

McKenzie, D., Bickle, M., 1988. The volume and composition of melt generated by extension of the lithosphere. J. Petrol. 29, 625–679. https://doi.org/10.1093/petrology/29.3.625.

Mosegaard, K., Tarantola, A., 2002. Probabilistic approach to inverse problems. In: International Handbook of Earthquake and Engineering Seismology. Academic Press, pp. 237–265.

Munch, F.D., Khan, A., Tauzin, B., van Driel, M., Giardini, D., 2020. Seismological evidence for thermo-chemical heterogeneity in Earth's continental mantle. Earth Planet. Sci. Lett. 539, 1–9. https://doi.org/10.1016/j.epsl.2020.116240.

Niazi, M., Anderson, D.L., 1965. Upper mantle structure of western North America from apparent velocities of P waves. J. Geophys. Res. 70, 4633–4640. https://doi.org/10.1029/JZ070i018p04633.

Ringwood, A.E., 1975. Composition and Petrology of the Earth's Mantle. McGraw-Hill, New York.

Schaeffer, A., Lebedev, S., 2013. Global shear speed structure of the upper mantle and transition zone. Geophys. J. Int. 194, 417–449. https://doi.org/10.1093/gji/ggt095.

Sigloch, K., 2011. Mantle provinces under North America from multifrequency P wave tomography. Geochem. Geophys. Geosyst. 12, 1–27. https://doi.org/10.1029/2010GC003421.

Silver, P.G., Carlson, R.W., Olson, P., 1988. Deep slabs, geochemical heterogeneity, and the large-scale structure of mantle convection: investigation of an enduring paradox. Annu. Rev. Earth Planet. Sci. 16, 477–541. https://doi.org/10.1146/annurev.ea.16.050188.002401.

Simmons, N.A., Forte, A.M., Boschi, L., Grand, S.P., 2010. GyPSuM: a joint tomographic model of mantle density and seismic wave speeds. J. Geophys. Res. 115. https://doi.org/10.1029/2010JB007631.

Sinha, G., Butler, S.L., 2007. On the origin and significance of subadiabatic temperature gradients in the mantle. J. Geophys. Res.

Stähler, S.C., Sigloch, K., Nissen-Meyer, T., 2012. Triplicated P-wave measurements for waveform tomography of the mantle transition zone. Solid Earth 3, 339–354. https://doi.org/10.5194/se-3-339-2012.

Stixrude, L., Lithgow-Bertelloni, C., 2005. Thermodynamics of mantle minerals - I. Physical properties. Geophys. J. Int. 162, 610–632. https://doi.org/10.1111/j.1365-246X.2005.02642.x.

Stixrude, L., Lithgow-Bertelloni, C., 2011. Thermodynamics of mantle minerals - II. Phase equilibria. Geophys. J. Int. 184, 1180–1213. https://doi.org/10.1111/j.1365-246X.2010.04890.x.

Tackley, P.J., 2000. Mantle convection and plate tectonics: toward an integrated physical and chemical theory. Science 288, 2002–2007. https://doi.org/10.1126/science.288.5473.2002.

Tajima, F., Katayama, I., Nakagawa, T., 2009. Variable seismic structure near the 660 km discontinuity associated with stagnant slabs and geochemical implications. Phys. Earth Planet. Inter. 172, 183–198. https://doi.org/10.1016/j.pepi.2008.09.013.

Tan, E., Gurnis, M., Han, L., 2002. Slabs in the lower mantle and their modulation of plume formation. Geochem. Geophys. Geosyst. 3. https://doi.org/10.1029/2001GC000238.

Tao, K., Grand, S.P., Niu, F., 2017. Full-waveform inversion of triplicated data using a normalized-correlation-coefficient-based misfit function. Geophys. J. Int. 210, 1517–1524. https://doi.org/10.1093/gji/ggx249.

Tauzin, B., Debayle, E., Wittlinger, G., 2008. The mantle transition zone as seen by global Pds phases: no clear evidence for a thin transition zone beneath hotspots. J. Geophys. Res. 113, 1–17. https://doi.org/10.1029/2007JB005364.

Tian, D., Lv, M., Wei, S., Dorfman, S.M., Shearer, P.M., 2020. Global variations of Earth's 520- and 560-km discontinuities. Earth Planet. Sci. Lett. 552. https://doi.org/10.1016/j.epsl.2020.116600.

Vallée, M., Douet, V., 2016. A new database of source time functions (STFs) extracted from the SCARDEC method. Phys. Earth Planet. Inter. 257, 149–157. https://doi.org/10.1016/j.pepi.2016.05.012.

van Driel, M., Krischer, L., Stähler, S.C., Hosseini, K., Nissen-Meyer, T., 2015. Instaseis: instant global seismograms based on a broadband waveform database. Solid Earth 6, 701–717. https://doi.org/10.5194/se-6-701-2015.

Weidner, D.J., 1985. A mineral physics test of a pyrolite mantle. Geophys. Res. Lett. 12, 417–420. https://doi.org/10.1029/GL012i007p00417.

White, W.M., 2010. Oceanic island basalts and mantle plumes: the geochemical perspective. Annu. Rev. Earth Planet. Sci. 38, 133–160. https://doi.org/10.1146/annurev-earth-040809-152450.

Wood, B.J., Holloway, J.R., 1984. A thermodynamic model for subsolidus equilibria in the system CaO–MgO–Al2O3–SiO2. Geochim. Cosmochim. Acta 48, 159–176. https://doi.org/10.1016/0016-7037(84)90358-2.

Wu, W., Ni, S., Irving, J.C.E., 2019. Inferring Earth's discontinuous chemical layering from the 660-kilometer boundary topography. Science 363, 736–740. https://doi.org/10.1126/science.aav0822.

Xu, W., Lithgow-Bertelloni, C., Stixrude, L., Ritsema, J., 2008. The effect of bulk composition and temperature on mantle seismic structure. Earth Planet. Sci. Lett. 275, 70–79. https://doi.org/10.1016/j.epsl.2008.08.012.

Yan, J., Ballmer, M.D., Tackley, P.J., 2020. The evolution and distribution of recycled oceanic crust in the Earth's mantle: insight from geodynamic models. Earth Planet. Sci. Lett. 537. https://doi.org/10.1016/j.epsl.2020.116171.

Zunino, A., Connolly, J.A.D., Khan, A., 2011. Pre-calculated phase equilibrium models for geophysical properties of the crust and mantle as a function of composition. Geochem. Geophys. Geosyst. 12. https://doi.org/10.1029/2010GC003304.